NANO LETTERS

pubs.acs.org/NanoLett Letter

Improving Photoelectric Conversion with Broadband Perovskite Metasurface

Jie He,[⊥] Cheng-Yao Li,[⊥] Dong-Xiang Qi, Qing Cai, Yu Liu, Ren-Hao Fan, Jing Su, Pengcheng Huo, Ting Xu, Ruwen Peng,* and Mu Wang*

Cite This: *Nano Lett.* 2022, 22, 6655−6663 Read Online

ACCESS | Metrics & More | Article Recommendations | Supporting Information

ABSTRACT: The miniaturization and integration of optoelectronic devices require progressive size reduction of active layers, resulting in less optical absorption and lower quantum efficiency. In this work, we demonstrate that introducing a metasurface made of hybrid organic−inorganic perovskite (HOIP) can significantly enhance broadband absorption and improve photon-to-electron conversion, which roots from exciting Mie resonances together with suppressing optical transmission. On the basis of the HOIP metasurface, a broadband photodetector has been fabricated where photocurrent boosts more than 10 times in the frequency ranging from ultraviolet to visible. The device response time is less than 5.1 μs at wavelengths 380, 532, and 710 nm, and the relevant 3 dB bandwidth is over 0.26 MHz. Moreover, this photodetector has been applied as a signal receiver for transmitting 2D color images in broadband optical communication. These results accentuate the practical applications of HOIP metasurfaces in novel optoelectronic devices for broadband optical communication.

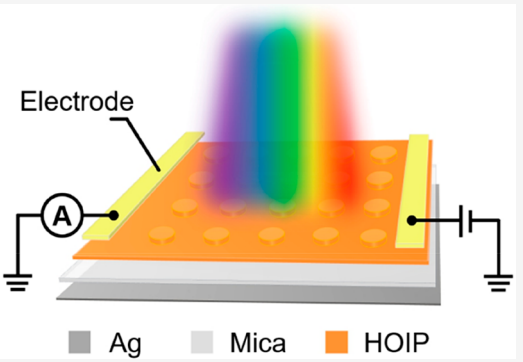

KEYWORDS: *Hybrid organic−inorganic perovskites, perovskite metasurfaces, broadband photodetector, light communication*

Hybrid organic−inorganic perovskites (HOIPs) have emerged as promising materials for advanced optoelectronic devices due to their ultralong carrier diffusion lengths, low incidence of trapping of defects and impurities, and high carrier mobility.[1−3] In the past few years, a series of perovskite-based optoelectronic devices have been proposed and experimentally demonstrated, such as photodetectors[4−7] and light-emitting diodes (LEDs).[8,9] The integration and miniaturization of advanced optoelectronic devices require a reduction of the thickness of the photoactive material, resulting in decreased absorption efficiency and lower external quantum efficiency.[10,11] To optimize the performance of perovskite-based devices, various schemes have been proposed to enhance the absorption of the active layers. Plasmonic nanoparticles or metasurfaces have been widely adopted because of their excited localized surface plasmon resonances,[12−15] despite suffering from metal losses. In addition, silicon or titanium dioxide dielectric resonators that can support Mie resonances have been introduced to produce near-field enhancement and promote light harvesting.[16,17] However, these methods increase the complexity and thickness of devices. More recently, HOIPs have also shown potential in all-dielectric metasurfaces owing to their high refractive index.[18] HOIP-based metasurfaces have been used to explore novel optical properties and realize various optoelectronic applications, such as resonantly enhanced absorption and fluorescence,[19−23] light-matter interaction,[23−27] high-resolution color,[28,29] and dynamic nanoprinting.[30] A few studies have also focused on photoelectric conversion and polarized light detection using perovskite metasurfaces.[31,32] Photoelectric devices based on perovskite metasurfaces are expected to improve the absorption of the active layers and the optoelectronic performance of devices. Such advances have rarely been reported, especially in practical optoelectronic applications such as light communication.

Here, we design and experimentally realize a broadband photodetector based on a perovskite metasurface. By introducing a perovskite metasurface and a bottom reflective mirror, the absorption of our HOIP metasurface is broadbandly enhanced in the wavelength range of 300−800 nm compared to that of the pure perovskite film. Subsequently, we fabricate a broadband photodetector based on this HOIP metasurface and characterize its photoelectrical performance. The photocurrent is enhanced under illumination with wavelengths ranging from ultraviolet to visible spectrum. Along with the rise/fall time measured as 4.1/3.6, 5.1/4.4, and 4.5/4.0 μs at wavelengths of 380, 532, and 710 nm,

Received: May 16, 2022
Revised: July 28, 2022
Published: August 4, 2022

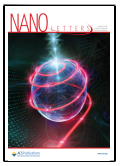

https://doi.org/10.1021/acs.nanolett.2c01979
Nano Lett. 2022, 22, 6655−6663

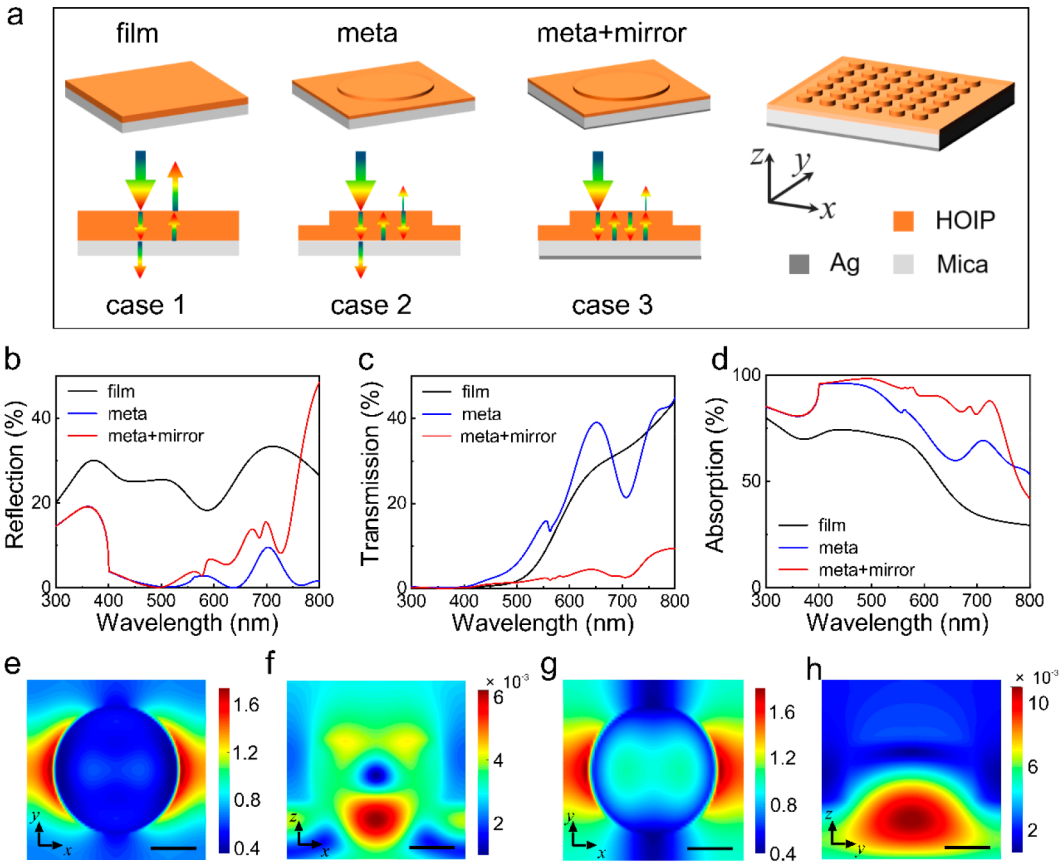

Figure 1. HOIP metasurface and its simulated optical response. (a) Schematic of absorption enhancement mechanisms and the designed HOIP metasurface sample; the diameter and the period of the nanodisks in the HOIP metasurface are 280 and 400 nm, respectively. (b–d) Simulated reflection (b), transmission (c), and absorption spectra (d) of pure film, metasurface, and metasurface with mirror, respectively. (e–h) Simulated electric field distributions in the *x*-*y* plane (e) and magnetic field distributions in the *x*-*z* plane (f) at the wavelength of 560 nm; Simulated electric field distributions in the *x*-*y* plane (g) and magnetic field distributions in the *y*-*z* plane (h) at the wavelength of 700 nm. The scale bars indicate 100 nm.

respectively, the proposed metasurface-based photodetector features a 3 dB bandwidth more than 0.26 MHz. Finally, we construct a broadband light communication system in which the proposed device functions as a light signal receiver. The experimental results demonstrate the transmission of ultraviolet and visible light signals, which suggests that HOIP metasurfaces possess the potential for promising future applications in light communication.

First, let us focus on the design of the HOIP metasurface. A schematic of the designed structure is illustrated in Figure 1a. In the configuration without a metasurface (Case 1), when light is incident on the flat perovskite film, some of the incident light is reflected vertically at the interface between air and the perovskite film. The perovskite film partially absorbs the rest of the incident light, and the unabsorbed light is transmitted through the sample. This leads to a low absorption efficiency of the perovskite film. To solve this problem, we introduce a metasurface on the perovskite film (Case 2). The metasurface composes of an array of HOIP nanodisks with identical periods in two orthogonal directions (*x* and *y*). The building block of the metasurface is a perovskite nanodisk located on top of the HOIP film on a mica substrate. We use the finite-difference time-domain simulation to optimize parameters of the height, diameter, and period of the disks, and then select the structure with the maximum light absorption (Supporting Information S1). Eventually the diameter and height of the nanodisks are chosen to be 280 and 100 nm, respectively. The period of the array is 400 nm. We simulate the reflection and transmission of the metasurface, as shown in Figure 1b,c, respectively. The optical constants of the HOIP ($CH_3NH_3PbI_3$) used in the simulation are obtained from the existing literature.[18] Compared with the pure flat film, the reflection of the metasurface is significantly suppressed owing to the introduction of the nanodisks, whereas the transmission does not change greatly. The absorption can be obtained from the reflection and transmission data using the relationship $A = 1 - R - T$, where *A*, *R*, and *T* denote absorbance, reflectance, and transmittance, respectively. As shown in Figure 1d, the absorption of the metasurface is enhanced in the wavelength range of 300–800 nm compared to that of the pure film. There are two resonance absorption peaks around 560 and 700 nm in the absorption spectra of the perovskite metasurface. To explore the origin of these two resonance absorption peaks, we calculate the corresponding electric and magnetic field distributions at these two resonance positions, as shown in Figure 1e–h. The resonance mode appearing at a wavelength of 560 nm is identified as an electric dipole mode, while the mode around 700 nm is derived from a magnetic dipole mode. By introducing the perovskite metasurface, absorption has been enhanced owing to reflection inhibition at the surface of

https://doi.org/10.1021/acs.nanolett.2c01979
Nano Lett. 2022, 22, 6655–6663

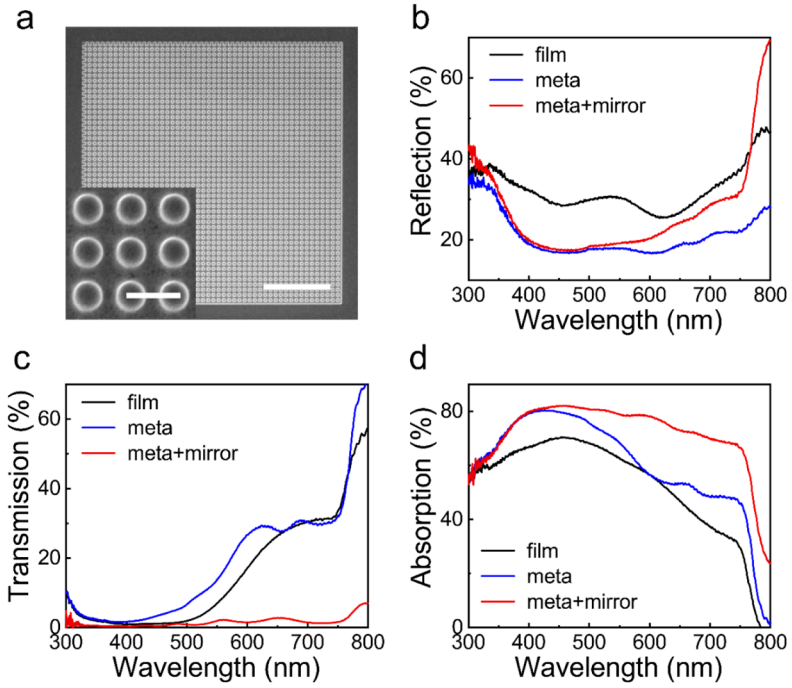

Figure 2. Experimentally measured optical spectra. (a) SEM images of the $MAPbI_3$ metasurface; the scale bar indicates 5 μm. The inset graph shows the magnified view of the metasurface; the scale bar indicates 500 nm. (b–d) Measured reflection (b), transmission (c), and absorption (d) spectra of pure film, metasurface, and metasurface with mirror, respectively.

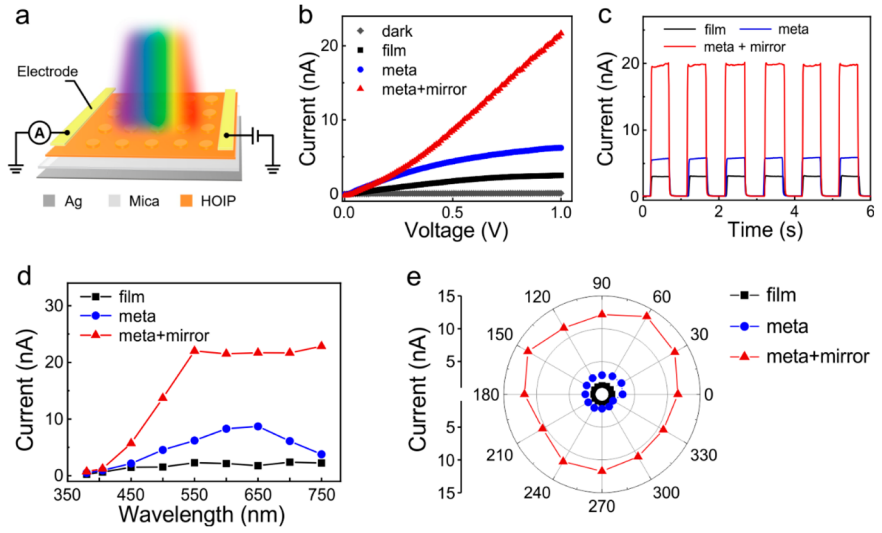

Figure 3. Photoelectrical performance of different samples. (a) Schematic of the photoelectrical measurement setup. (b) The I–V curves of pure film, metasurface, and metasurface with mirror, respectively, illuminated by a 700 nm laser. (c) The on/off switching performance of the pure film, metasurface, and metasurface with mirror, respectively. (d) The photocurrent of pure film, metasurface, and metasurface with mirror, respectively, under illumination at different wavelengths under a voltage of 1 V. (e) The polarization independence of photocurrents of pure film, metasurface, and metasurface with mirror, respectively, at a voltage of 1 V and illuminated by a 700 nm laser. In all cases, the power density of laser illumination is 3.3×10^2 W/cm^2.

the perovskite flat film and resonances excited in the metasurface. Similar reflection suppression effects have also been achieved in other perovskite metasurfaces. For example, Baryshnikova et al.[19] proposed to employ the Kerker conditions for halide perovskite metasurfaces to achieve broadband suppression of reflection. Furthermore, the absorption can be further enhanced because a considerable portion of the transmitted light is not absorbed in Case 2, resulting in a reduced energy conversion efficiency of the incident light. Therefore, we design a sample that includes a bottom mirror as a reflective layer in addition to the metasurface by depositing 35 nm of silver on the back of the mica structure, which is depicted as Case 3 in Figure 1a. In this case, the existence of the back-reflective layer reflects the unabsorbed transmitted light. This structure allows the perovskite layer to reabsorb the light to improve absorption further. From the reflection and transmission spectra, we can observe that compared with a pure flat film and metasurface,

https://doi.org/10.1021/acs.nanolett.2c01979
Nano Lett. 2022, 22, 6655–6663

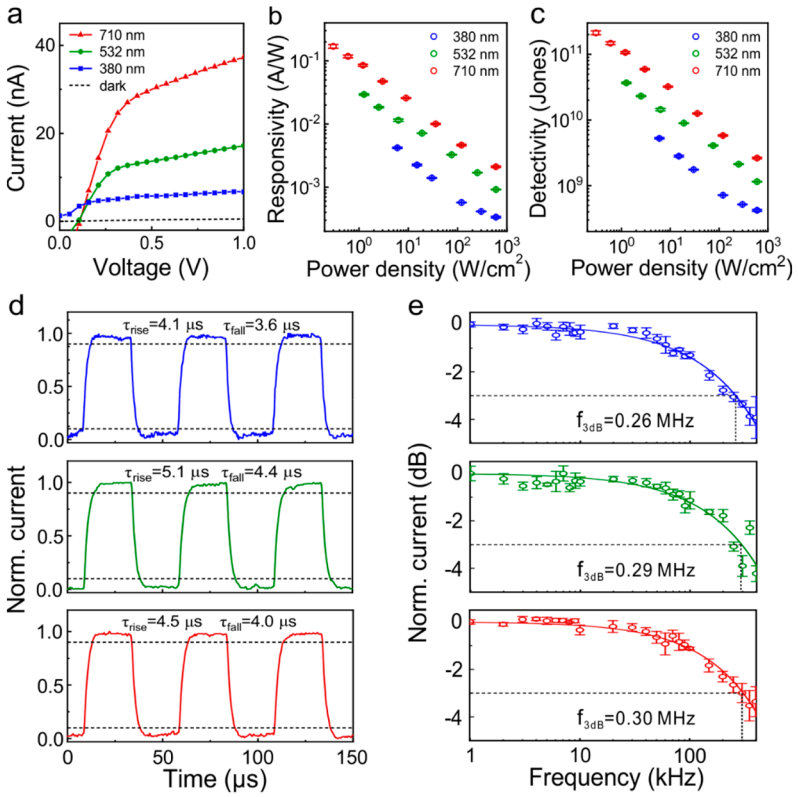

Figure 4. Broadband photodetection performance of HOIP metasurface. (a) Measured $I-V$ curves under 380, 532, and 710 nm laser illumination with a power density of 6.0×10^2 W/cm^2 and dark conditions. (b) Responsivity at different wavelengths versus incident power density at a voltage of 1 V. (c) The detectivity of the photodetector at three different wavelengths. (d) Time-resolved photocurrent response under 20 kHz modulated 380 nm (upper panel), 532 nm (middle panel), and 710 nm (lower panel) illumination at a voltage of 5 V. (e) Normalized response as a function of input signal frequency under 380 nm (upper panel), 532 nm (middle panel), and 710 nm (lower panel) illumination, showing the 3 dB bandwidth of the device.

the transmittance is sharply reduced by introducing a back-reflected silver film, whereas the reflectance is only enhanced slightly, which results in a substantial increase in absorption associated with this structure.

Experimentally, we first grow a single-crystal $CH_3NH_3PbI_3$ ($MAPbI_3$) film on a freshly cleaved mica substrate via a quasi-static solution growth process.[5,33,34] The designed HOIP metasurface is fabricated by etching a 200 nm thick $MAPbI_3$ film using focused ion beam (FIB) milling with an etching depth of approximately 100 nm. The scanning electron microscopy (SEM) images of the HOIP metasurface are depicted in Figure 2a. The square area of the metasurface is about 20×20 μm^2. The measured reflection, transmission, and absorption spectra are shown in Figure 2b–d, respectively. These experimental results are similar to the simulated spectra in Figure 1, indicating that absorption was broadband-enhanced in the wavelength range of 300–800 nm compared to the pure perovskite film by introducing a perovskite metasurface and bottom reflective mirror. Besides, we also characterized the electrical properties of the perovskite material before and after FIB processing, showing no significant change in the electrical properties of the samples (Supporting Information S2).

Because absorption in perovskite film has been greatly enhanced by introducing a metasurface and bottom reflective mirror layer, we expect that the photoelectric performance of the HOIP metasurface might be subsequently improved. To measure the photoelectrical response of different samples, we fabricate a pair of gold electrodes by evaporating 40 nm of Au on both sides of the perovskite metasurface, as schematically shown in Figure 3a. The distance between the Au electrodes is approximately 60 μm. The photoelectrical performance of the samples under 700 nm laser illumination is characterized by a source meter. The size of the illumination spot is approximately 3 μm^2. The power density is kept as 3.3×10^2 W/cm^2. The measured $I-V$ curves of the three samples (pure perovskite film, perovskite metasurface, and metasurface with mirror) are depicted in Figure 3b. The photoresponse of the sample is increased by introducing a metasurface. Photocurrent of the metasurface with a mirror is further promoted over 10-fold compared with that in pure perovskite film at the voltage of 1 V, benefiting from exciting resonance modes in the perovskite metasurface and suppressing the reflection and transmission. In addition, we measure the switching response of the device at a voltage of 1 V, as shown in Figure 3c. The on–off ratio of the pure film, metasurface, and metasurface with mirror are about 24, 42, and 173, respectively. Subsequently, we measure the photocurrent at different wavelengths under a voltage of 1 V, as shown in Figure 3d. It is observed that the photoelectrical performance of the metasurface with a mirror is considerably better than that of the pure film. The photoresponse is enhanced at the wavelengths from 380 to 750 nm, indicating that our metasurface offers broadband photocurrent enhancement. The dependence on the incident light polarization is also examined. Figure 3e shows the polarization independence of

https://doi.org/10.1021/acs.nanolett.2c01979
Nano Lett. 2022, 22, 6655–6663

Table 1. Comparison of the Performance of the Proposed Metasurface Photodetector with That of Previously Reported Planar-Type Photodetectors

material	material structure	thickness of active layer	spectral range [nm]	illuminating conditions	responsivity [A/W]	rise/fall time [s]	ref
Se/Si	micrometer-sized crystal		350−690	0.704 mW/cm^2@610 nm@-2 V	3.74×10^{-2}	$0.24/1.74 \times 10^{-3}$	38
GaSe	flake	26 nm	∼200−700	0.07 mW/cm^2@380 nm@5 V	2.6	0.7/1.2	39
MoS_2	microspheres		405−808	1.77 mW/cm^2@405 nm@1 V	0.963	9.33/12.67	40
MoS_2 /GaN	heterostructure	∼3.5 μm	280−850	2 mW/cm^2@365 nm@1 V	12.61×10^3	∼0.1/0.6	41
				2 mW/cm^2@565 nm@1 V	3.98×10^3		
				2 mW/cm^2@850 nm@1 V	80		
$SnSe_2$ /SnO_2	quantum dots on nanoflakes	∼49 nm	∼250−800	14.6 μW/cm^2@365 nm@2 V	4.79×10^{-2}	0.5	42
				23.8 μW/cm^2@554 nm@2 V	1.68×10^{-2}	0.5	
				27.63 μW/cm^2@780 nm@2 V	6.51×10^{-3}	0.93	
$CsPbBr_3$	microcrystals		∼350−505	0.1 mW/cm^2@505 nm@5 V	2300	$1.3/2.2 \times 10^{-2}$	37
$MAPbBr_3$	nanosheet	∼20 nm	∼400−520	0.08 mW/cm^2@514 nm@1 V	∼5600	$3.2/9.2 \times 10^{-6}$	5
$MAPbI_3$	porous films	∼1 μm	410−710	0.001 mW/cm^2 @white light@2 V	2.73	$<5 \times 10^{-3}$	43
$MAPbI_3$	nanoribbon arrays	∼70 nm	300−800	38.5 μW/cm^2@300 nm@2 V	3.89×10^{-2}	$2.7/2.6 \times 10^{-2}$	44
$MAPbI_3$	nanorods		350−950	0.18 mW/cm^2@405 nm@4 V	1.2×10^{-2}	$1.8/2.5 \times 10^{-2}$	45
$MAPbI_3$	metasurface integrated with film	200 nm	380−750	0.3 W/cm^2@710 nm@1 V	0.17	$4.5/4.0 \times 10^{-6}$	this work
				1.3 W/cm^2@532 nm@1 V	0.03	$5.1/4.4 \times 10^{-6}$	
				6 W/cm^2@380 nm@1 V	4×10^{-3}	$4.1/3.6 \times 10^{-6}$	

photocurrents in pure film, metasurface, and metasurface with a mirror, respectively (Here 0° indicates linear polarization along the x-direction). We conclude that the photocurrent enhancement can be achieved under various linearly polarized light illumination. The reason is that our metasurface is composed of nanodisks with the same periodicity in both x and y directions, and the absorption enhancement is insensitive to the incident polarization.

The photoelectrical performance of the device made of the HOIP metasurface has been improved across a broadband wavelength range. Then we apply the device as a broadband photodetector. The $I-V$ curves under illumination at different wavelengths are depicted in Figure 4a. The photocurrent reaches 38 nA at a voltage of 1 V when a 710 nm laser illuminates the sample with a power density of 6.0×10^2 W/cm^2. The dark current is 0.55 nA, and the corresponding on−off ratio is approximately 70. Under the same conditions, the photocurrents are 7 and 17 nA at the illumination with the wavelength of 380 and 532 nm, respectively. The responsivity is an essential parameter describing the efficiency of photodetectors, and it is defined as $R = \frac{I_{photo} - I_{dark}}{P_{inc}}$, where I_{photo} and I_{dark} are the photocurrent and dark current of the device, respectively, and P_{inc} is the power of the incident light detected by the photodetector. The responsivity of the proposed device reaches 170 mA/W under 710 nm laser illumination (0.3 W/cm^2), as shown in Figure 4b. Meanwhile the responsivities are 30 mA/W at 532 nm with a power density of 1.3 W/cm^2 and 4 mA/W at 380 nm with a power density of 6 W/cm^2. Furthermore, as shown in Figure 4c, we also characterize the detectivity $D^* = \frac{R}{(2eJ_{dark})^{1/2}}$ where R is the responsivity, e is the elementary charge, and J_{dark} is dark current density of the device.

The response speed of a photodetector is also crucial for potential applications such as light communication. To determine the response time of our device, we use an acousto-optic modulator to modify the incident light. As shown in Figure 4d, the photocurrents increase and decay with modulated light. The rise (fall) time of our device is defined as the response time for the photocurrent to change from 10% (90%) to 90% (10%). The rise (fall) time is 4.5 (4.0) μs under 20 kHz modulated 710 nm illumination. The results for 380 and 532 nm incident light are 4.1 (3.6) μs and 5.1 (4.4) μs, respectively, demonstrating the short response time of our device for broadband light detection. We also examine the 3 dB bandwidth of our device (as shown in Figure 4e), defined as the frequency range of the modulated incident light across which the photocurrent of the device reaches at least half of its maximum value. The 3 dB bandwidths of our device are estimated as 0.26, 0.29, and 0.30 MHz for 380, 532, and 710 nm light, respectively, implying a rapid response to the modulated light signal from the ultraviolet to the visible spectrum.

We compare our photodetector with recently reported planar-type photodetectors operating in the ultraviolet and visible regions (summarized in Table 1). Our photodetector based on the perovskite metasurface exhibits the following characteristics: (i) The thickness of the active layer is down to 200 nm, which meets the requirement of the integration and compactification of elements in circuits. (ii) The spectral range of our photodetector covers the visible and ultraviolet regions, which is comparable to most of the detectors in Table 1. (iii) The corresponding responsivity is higher than those of the plasmonic metasurface photodetectors,[35,36] although lower than those of highly sensitive single-crystal bromide-based perovskite photodetectors. Moreover, compared with these photodetectors with high responsivity based on perovskite thin films,[5,37] the photodetector based on perovskite metasurface in

https://doi.org/10.1021/acs.nanolett.2c01979
Nano Lett. 2022, 22, 6655−6663

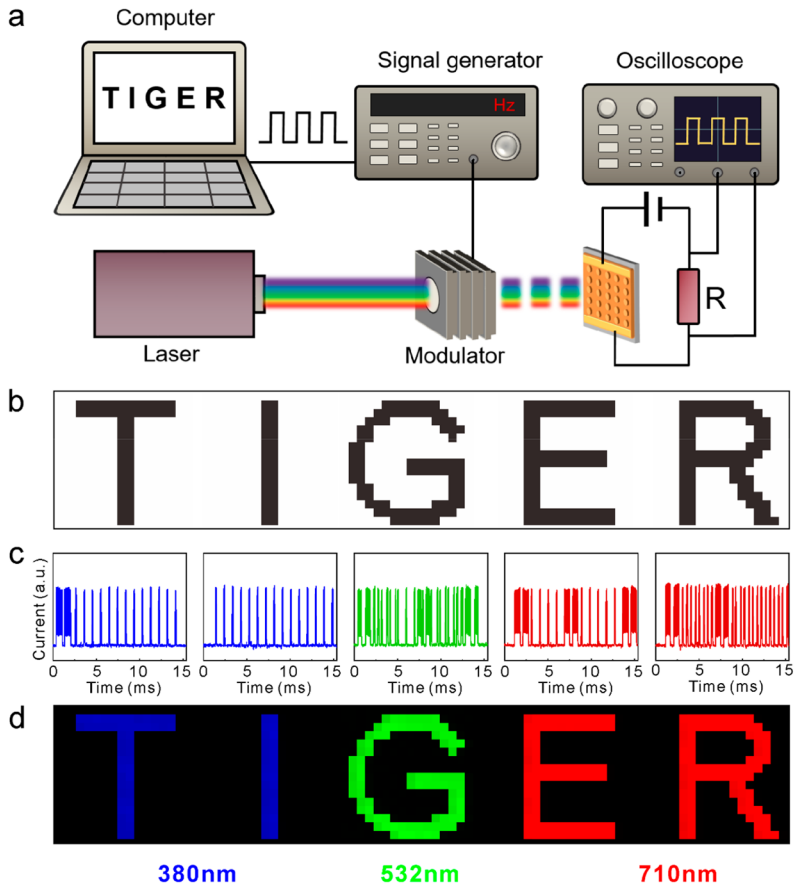

Figure 5. Light communication system based on HOIP metasurface photodetector. (a) Schematic of light communication setup. (b) 16 × 16 pixel images of letters "T" "I" "G" "E" and "R" that we input. (c) Waveforms of output current signals correspond to five images, here time to transmit each pixel is 60 μs. (d) 2D color images of letters reproduced from current waveforms generated by HOIP metasurface based photodetector.

our work has a long distance between the gold electrodes due to the existence of metasurface, which affects the transmission of photoinduced carriers, resulting in reduced responsivity. This effect has also been reported previously in polarization detectors based on perovskite metasurfaces.[32] (iv) The response time is shorter than 5.1 μs at three different wavelengths, which corresponds to a 3 dB bandwidth higher than 0.26 MHz. Such response time is shorter than those of the detectors[37−45] in Table 1. The rapid response of the device at different wavelengths demonstrates its potential for high-speed detection in the ultraviolet and visible spectra and broadband optical communications. In addition, the stability of our device (Supporting Information S3) is comparable to those of hybrid perovskite thin-film devices. Yet our organic−inorganic hybrid materials are less stable than inorganic perovskite materials[26,27] and silicon-based[38] devices.

It is known that optical communication systems rely on light with wavelengths ranging from the ultraviolet domain to the infrared to convey information. Because the proposed device can collect both ultraviolet and visible light and generate photoinduced carriers, we design a broadband light communication system in which this device can function as a broadband light signal receiver. A schematic of the proposed light-communication system is shown in Figure 5a. We attempt to transmit five 16 × 16 pixel color images of five letters: ultraviolet "T" and "I", green "G", red "E" and "R". First, two states ("ON" and "OFF") of each pixel in a two-dimensional image are represented by high and low voltage levels. Then five 16 × 16 arrays of voltage levels are converted into five 256-element sequences that represent five letters. These sequences are used to switch the voltage level temporally. The acoustic optical modulator is subsequently controlled by the voltage-level sequence and transfers continuous illumination into a temporally modulated light signal, where the sequence in the time domain is identical to the temporal sequence of the voltage level. Next, the HOIP metasurface-based photodetector captures the light signal and generates photocurrent with a specified waveform. Finally, the current waveform is monitored using an oscilloscope with the load resistance. The waveform is processed into a 256-element sequence and reshaped into a 16 × 16 array by a computer to obtain the input image. The input images with 16 × 16 pixels representing the letters "T" "I" "G" "E" and "R" are illustrated in Figure 5b. The information in these images is transmitted using our light communication system. The current waveforms generated by the photodetector after collecting the light signals are shown in Figure 5c. The time required to transmit each pixel of the images is 60 μs; therefore, the corresponding transmission rate is 16.67 kHz. The corresponding 2D color images reproduced from the current waveform are shown in Figure 5d. The letters in different colors are transmitted by three different lights with wavelengths ranging from ultraviolet to visible spectrum. This result demonstrates that our device can be used as a broadband light signal receiver and shows promise for future applications in light communications.

https://doi.org/10.1021/acs.nanolett.2c01979
Nano Lett. 2022, 22, 6655−6663

In conclusion, we design a HOIP metasurface and fabricate the sample using focused ion beam milling. The broadband absorption enhancement is proved experimentally, and the photocurrent is increased more than 10-fold. The proposed device demonstrates exemplary performance and rapid response across the visible and ultraviolet spectra. Finally, we use this device as a signal receiver and verify a broadband light communication system. Our results demonstrate the practical applicability of HOIP metasurfaces in photon-to-electron conversion devices and their promising potential for enhanced light communication.

METHODS

Simulation. In the simulation, periodic boundary conditions in the *x*- and *y*-directions and perfectly matched layer (PML) boundary conditions in the *z*-direction are applied. Plane-wave sources with wavelengths in the range 300−800 nm are placed 1 μm from the structure. As the diameter and period are symmetric on the *x*-axis and *y*-axis, the metasurface is equivalent for both transverse magnetic (TM-) and transverse electric (TE-) polarized electromagnetic waves for normal incident light. The incident light is incident normally with polarization along the *x*-direction.

Metasurface Fabrication. Single crystal $MAPbI_3$ films with a thickness of 200 nm are grown on a cleaned mica substrate using a method reported previously. The metasurface is fabricated by etching the grown perovskite film for 5 min with the dual-beam FIB system (Helios, Nanolab 600i) under an operating current of 7.7 pA and an operating voltage of 30 kV. In addition, a reflective mirror is deposited on the back of the mica substrate using electron-beam evaporation.

Optical Properties. Steady-state reflection and transmission spectra are obtained using a microspectrophotometer (CRAIC Technologies, 20/30PV). Spectra are collected with a 40× objective lens over an area of 25 μm^2.

Photoelectric Measurements. The photoelectric performance is measured using a program-controlled source-meter system (Keithley 2636 B). A wavelength-tunable Ti:sapphire laser (Mai Tai, HP) and a supercontinuum white light laser (NKT Photonics, SuperK Fianium FIU-15) are used as the light sources. In addition, the time-dependent responses are recorded using a digital oscilloscope (Tektronix, TDS2022C) with an input impedance of 50 MΩ. The waveform and frequency of the input light are manipulated using a computer-controlled signal generator and acoustic-optical modulator. Additional resistors are used to monitor the currents in the circuit.

ASSOCIATED CONTENT

Supporting Information

The Supporting Information is available free of charge at https://pubs.acs.org/doi/10.1021/acs.nanolett.2c01979.

Structural parameter optimization, material characteization and electrical properties, and device stability testing (PDF)

AUTHOR INFORMATION

Corresponding Authors

Ruwen Peng − *National Laboratory of Solid State Microstructures, School of Physics, and Collaborative Innovation Center of Advanced Microstructures, Nanjing University, Nanjing 210093, China;* orcid.org/0000-0003-0424-2771; Email: rwpeng@nju.edu.cn

Mu Wang − *National Laboratory of Solid State Microstructures, School of Physics, and Collaborative Innovation Center of Advanced Microstructures, Nanjing University, Nanjing 210093, China; American Physical Society, Ridge, New York 11961, United States;* Email: muwang@nju.edu.cn

Authors

Jie He − *National Laboratory of Solid State Microstructures, School of Physics, and Collaborative Innovation Center of Advanced Microstructures, Nanjing University, Nanjing 210093, China*

Cheng-Yao Li − *National Laboratory of Solid State Microstructures, School of Physics, and Collaborative Innovation Center of Advanced Microstructures, Nanjing University, Nanjing 210093, China*

Dong-Xiang Qi − *National Laboratory of Solid State Microstructures, School of Physics, and Collaborative Innovation Center of Advanced Microstructures, Nanjing University, Nanjing 210093, China*

Qing Cai − *National Laboratory of Solid State Microstructures, School of Physics, and Collaborative Innovation Center of Advanced Microstructures, Nanjing University, Nanjing 210093, China*

Yu Liu − *National Laboratory of Solid State Microstructures, School of Physics, and Collaborative Innovation Center of Advanced Microstructures, Nanjing University, Nanjing 210093, China*

Ren-Hao Fan − *National Laboratory of Solid State Microstructures, School of Physics, and Collaborative Innovation Center of Advanced Microstructures, Nanjing University, Nanjing 210093, China*

Jing Su − *School of Physics and Optoelectronic Engineering, Nanjing University of Information Science and Technology, Nanjing 210044, China;* orcid.org/0000-0002-1812-5026

Pengcheng Huo − *National Laboratory of Solid-State Microstructures, College of Engineering and Applied Sciences, and Collaborative Innovation Center of Advanced Microstructures, Nanjing University, Nanjing 210093, China*

Ting Xu − *National Laboratory of Solid-State Microstructures, College of Engineering and Applied Sciences, and Collaborative Innovation Center of Advanced Microstructures, Nanjing University, Nanjing 210093, China;* orcid.org/0000-0002-0704-1089

Complete contact information is available at: https://pubs.acs.org/10.1021/acs.nanolett.2c01979

Author Contributions

[⊥]J.H. and C.Y.L. contributed equally to this work.

Author Contributions

R.P., J.H., C.Y.L., and M.W. conceived this work. C.Y.L. and J.H. fabricated the device with the assistance of Q.C. and Y.L.; J.H., C.Y.L., and P.H. performed the optical experiments with the help of R.H.F. and T.X.; J.H. performed the electrical experiments with the help of D.X.Q.; C.Y.L. and Q.C. provided the precursor solution with the help of J.S.; R.P. and M.W. directed the experiments. C.Y.L., J.H., R.P., and M.W. wrote the manuscript.

https://doi.org/10.1021/acs.nanolett.2c01979
Nano Lett. 2022, 22, 6655−6663

Notes

The authors declare no competing financial interest.

■ ACKNOWLEDGMENTS

This work was supported by the National Key R&D Program of China (2020YFA0211300, 2017YFA0303702), and by the National Natural Science Foundation of China (Grants 61975078, 11974177, and 11634005). We appreciate Prof. D. Wu and S. Qiu for the XRD measurements.

■ REFERENCES

(1) Sutherland, B. R.; Sargent, E. H. Perovskite photonic sources. *Nat. Photonics* **2016**, *10*, 295−302.
(2) Chen, Y.; Yi, H. T.; Wu, X.; Haroldson, R.; Gartstein, Y. N.; Rodionov, Y. I.; Tikhonov, K. S.; Zakhidov, A.; Zhu, X. Y.; Podzorov, V. Extended carrier lifetimes and diffusion in hybrid perovskites revealed by Hall effect and photoconductivity measurements. *Nat. Commun.* **2016**, *7*, 12253.
(3) Long, G.; Sabatini, R.; Saidaminov, M. I.; Lakhwani, G.; Rasmita, A.; Liu, X.; Sargent, E. H.; Gao, W. Chiral-perovskite optoelectronics. *Nat. Rev. Mater.* **2020**, *5*, 423.
(4) García de Arquer, F. P.; Armin, A.; Meredith, P.; Sargent, E. H. Solution processed semiconductors for next-generation photodetectors. *Nat. Rev. Mater.* **2017**, *2*, 16100.
(5) Jing, H.; Peng, R. W.; Ma, R.-M.; He, J.; Zhou, Y.; Yang, Z. Q.; Li, C.-Y.; Liu, Y.; Guo, X. J.; Zhu, Y. Y.; Wang, D.; Su, J.; Sun, C.; Bao, W. Z.; Wang, M. Flexible Ultrathin Single-Crystalline Perovskite Photodetector. *Nano Lett.* **2020**, *20*, 7144.
(6) Yang, Z.; Deng, Y.; Zhang; Wang, S.; Chen, H.; Yang, S.; Khurgin, J.; Fang, N. X.; Zhang, X.; Ma, R. High-performance single-crystalline perovskite thin-film photodetector. *Adv. Mater.* **2018**, *30*, 1704333.
(7) Li, C. Y.; He, J.; Zhou, Y.; Qi, D. X.; Jing, H.; Su, J.; Peng, R. W.; Fan, R. H.; Huo, P.; Xu, T.; Wang, M. Flexible perovskite nanosheet-based photodetectors for ultraviolet communication applications. *Appl. Phys. Lett.* **2021**, *119* (25), 251105.
(8) Lin, K.; Xing, J.; Quan, L. N.; Arquer, F. P. G.; Gong, X.; Lu, J.; Xie, L.; Zhao, W.; Zhang, D.; Yan, C.; Li, W.; Liu, X.; Lu, Y.; Kirman, J.; Sargent, E. H.; Xiong, Q.; Wei, Z. Perovskite light-emitting diodes with external quantum efficiency exceeding 20%. *Nature* **2018**, *562*, 245.
(9) Cao, Y.; Wang, N.; Tian, H.; Guo, J.; Wei, Y.; Chen, H.; Miao, Y.; Zou, W.; Pan, K.; He, Y.; Cao, H.; Ke, Y.; Xu, M.; Wang, Y.; Yang, M.; Du, K.; Fu, Z.; Kong, D.; Dai, D.; Jin, Y.; Li, G.; Li, H.; Peng, Q.; Wang, J.; Huang, W. Perovskite light-emitting diodes based on spontaneously formed submicrometre-scale structures. *Nature* **2018**, *562*, 249.
(10) Chen, Y. X.; Ge, Q. Q.; Shi, Y.; Liu, J.; Xue, D. J.; Ma, J. Y.; Ding, J.; Yan, H. J.; Hu, J. S.; Wan, L. J. General Space-Confined On-Substrate Fabrication of Thickness-Adjustable Hybrid Perovskite Single-Crystalline Thin Films. *J. Am. Chem. Soc.* **2016**, *138* (50), 16196−16199.
(11) Zhu, L. H.; Shao, M. R.; Peng, R. W.; Fan, R. H.; Huang, X. R.; Wang, M. Broadband absorption and efficiency enhancement of an ultra-thin silicon solar cell with a plasmonic fractal. *Opt. Express* **2013**, *21* (S3), A313−A323.
(12) Lu, L.; Luo, Z.; Xu, T.; Yu, L. Cooperative plasmonic effect of Ag and Au nanoparticles on enhancing performance of polymer solar cells. *Nano Lett.* **2013**, *13* (1), 59−64.
(13) Wu, J. L.; Chen, F. C.; Hsiao, Y. S.; Chien, F. C.; Chen, P.; Kuo, C. H.; Huang, M. H.; Hsu, C. S. Surface plasmonic effects of metallic nanoparticles on the performance of polymer bulk heterojunction solar cells. *ACS Nano* **2011**, *5* (2), 959−967.
(14) He, J.; Zhou, Y.; Li, C.-Y.; Xiong, B.; Jing, H.; Peng, R.; Wang, M. Metasurface-assisted broadband optical absorption in ultrathin perovskite films. *Opt. Express* **2021**, *29*, 19170−19182.
(15) Du, B.; Yang, W.; Jiang, Q.; Shan, H.; Luo, D.; Li, B.; Tang, W.; Lin, F.; Shen, B.; Gong, Q.; Zhu, X.; Zhu, R.; Fang, Z. Plasmonic-Functionalized Broadband Perovskite Photodetector. *Adv. Opt. Mater.* **2018**, *6*, 1701271.
(16) Tiguntseva, E.; Chebykin, A.; Ishteev, A.; Haroldson, R.; Balachandran, B.; Ushakova, E.; Komissarenko, F.; Wang, H.; Milichko, V.; Tsypkin, A.; Zuev, D.; Hu, W.; Makarov, S.; Zakhidov, A. Resonant silicon nanoparticles for enhancement of light absorption and photoluminescence from hybrid perovskite films and metasurfaces. *Nanoscale* **2017**, *9* (34), 12486−12493.
(17) Brongersma, M. L.; Cui, Y.; Fan, S. Light management for photovoltaics using high-index nanostructures. *Nat. Photonics* **2014**, *13* (5), 451−460.
(18) Green, M. A.; Jiang, Y. J.; Soufiani, A. M.; Ho-Baillie, A.W.-Y. Optical properties of photovoltaic organic-inorganic lead halide perovskites. *J. Phys. Chem. Lett.* **2015**, *6*, 4774.
(19) Baryshnikova, K.; Gets, D.; Liashenko, T.; Pushkarev, A.; Mukhin, I.; Kivshar, Y.; Makarov, S. Broadband antireflection with halide perovskite metasurfaces. *Laser & Photonics Reviews* **2020**, *14*, 2000338.
(20) Fan, Y. B.; Wang, Y. H.; Zhang, N.; Sun, W. Z.; Gao, Y. S.; Qiu, C.-W.; Song, Q. H.; Xiao, S. M. Resonance-enhanced three-photon luminesce via lead halide perovskite metasurfaces for optical encoding. *Nat. Commun.* **2019**, *10*, 2085.
(21) Makarov, S. V.; Milichko, V.; Ushakova, E. V.; Omelyanovich, M.; Pasaran, A. C.; Haroldson, R.; Balachandran, B.; Wang, H. L.; Hu, W.; Kivshar, Y. S.; Zakhidov, A. A. Multifold Emission Enhancement in Nanoimprinted Hybrid Perovskite Metasurfaces. *ACS Photonics* **2017**, *4*, 728.
(22) Kessel, A.; Frydendahl, C.; Indukuri, S. R. K. C.; Mazurski, N.; Arora, P.; Levy, U. Soft Lithography for Manufacturing Scalable Perovskite Metasurfaces with Enhanced Emission and Absorption. *Adv. Opt. Mater.* **2020**, *8*, 2001627.
(23) Wang, H. L.; Liu, S.-C.; Balachandran, B.; Moon, J.; Haroldson, R.; Li, Z. T.; Ishteev, A.; Gu, Q.; Zhou, W. D.; Zakhidov, A.; Hu, W. Nanoimprinted perovskite metasurface for enhanced photoluminescence. *Opt. Express* **2017**, *25*, A1162.
(24) Dang, N. H. M.; Gerace, D.; Drouard, E.; Trippé-Allard, G.; Lédée, F.; Mazurczyk, R.; Deleporte, E.; Seassal, C.; Nguyen, H. S. Tailoring Dispersion of Room-Temperature Exciton-Polaritons with Perovskite-Based Subwavelength Metasurfaces. *Nano Lett.* **2020**, *20*, 2113.
(25) Tiguntseva, E. Y.; Baranov, D. G.; Pushkarev, A. P.; Munkhbat, B.; Komissarenko, F.; Franckevicius, M.; Zakhidov, A. A.; Shegai, T.; Kivshar, Y. S.; Makarov, S. V. Tunable hybrid Fano resonances in halide perovskite nanoparticles. *Nano Lett.* **2018**, *18*, 5522−5529.
(26) Su, R.; Ghosh, S.; Wang, J.; Liu, S.; Diederichs, C.; Liew, T. C. H.; Xiong, Q. Observation of exciton polariton condensation in a perovskite lattice at room temperature. *Nat. Phys.* **2020**, *16*, 301−306.
(27) Su, R.; Ghosh, S.; Liew, T. C. H.; Xiong, Q. Optical switching of topological phase in a perovskite polariton lattice. *Sci. Adv.* **2021**, *7*, eabf8049.
(28) Gholipour, B.; Adamo, G.; Cortecchia, D.; Krishnamoorthy, H. N. S.; Birowosuto, M. D.; Zheludev, N. I.; Soci, C. Organometallic perovskite metasurfaces. *Adv. Mater.* **2017**, *29*, 1604268.
(29) Gao, Y.; Huang, C.; Hao, C.; Sun, S.; Zhang, L.; Zhang, C.; Duan, Z.; Wang, K.; Jin, Z.; Zhang, N.; Kildishev, A. V.; Qiu, C.-W.; Song, Q.; Xiao, S. Lead halide perovskite nanostructures for dynamic color display. *ACS Nano* **2018**, *12*, 8847.
(30) Zhang, C.; Xiao, S.; Wang, Y.; Gao, Y.; Fan, Y.; Huang, C.; Zhang, N.; Yang, W.; Song, Q. Lead Halide Perovskite-Based Dynamic Metasurfaces. *Laser & Photonics Reviews* **2019**, *13*, 1900079.
(31) Jing, H.; Zhu, Y. Y.; Peng, R.-W.; Li, C.-Y.; Xiong, B.; Wang, Z.; Liu, Y.; Wang, M. Hybrid organic-inorganic perovskite metamaterial for light trapping and photon-to-electron conversion. *Nanophotonics* **2020**, *9*, 3323.
(32) Li, C. Y.; Chen, C.; Liu, Y.; Su, J.; Qi, D.-X.; He, J.; Fan, R. H.; Cai, Q.; Li, Q.; Peng, R.; Huang, X. R.; Wang, M. Multiple-polarization-sensitive photodetector based on a perovskite metasurface. *Opt. Lett.* **2022**, *47* (3), 565−568.

https://doi.org/10.1021/acs.nanolett.2c01979
Nano Lett. 2022, 22, 6655−6663

(33) Zhang, B. B.; Weng, Y.-Y.; Huang, X.-P.; Wang, M.; Peng, R.-W.; Ming, N.-B.; Yang, B. J.; Lu, N.; Chi, L. F. Creating In-Plane Metallic-Nanowire Arrays by Corner-Mediated Electrodeposition. *Adv. Mater.* **2009**, *21*, 3576.
(34) Wang, D.; Shi, W.-B.; Jing, H.; Yin, C.; Zhu, Y.; Su, J.; Ma, G.-B.; Peng, R.; Wang, X.; Wang, M. Photon-induced carrier recombination in the non-layered-structured hybrid organic-inorganic perovskite nano-sheets. *Opt. Express* **2018**, *26*, 27504.
(35) Venuthurumilli, P. K.; Ye, P. D.; Xu, X. F. Plasmonic Resonance Enhanced Polarization-Sensitive Photodetection by Black Phosphorus in Near Infrared. *ACS Nano* **2018**, *12*, 4861.
(36) Li, W.; Coppens, Z. J.; Besteiro, L. V.; Wang, W. Y.; Govorov, A. O.; Valentine, J. Circularly polarized light detection with hot electrons in chiral plasmonic metamaterials. *Nat. Commun.* **2015**, *6*, 8379.
(37) Marunchenko, A. A.; Baranov, M. A.; Ushakova, E. V.; Ryabov, D. R.; Pushkarev, A. P.; Gets, D. S.; Nasibulin, A. G.; Makarov, S. V. Single-walled carbon nanotube thin film for flexible and highly responsive perovskite photodetector. *Adv. Funct. Mater.* **2022**, *32*, 2109834.
(38) Yang, W.; Hu, K.; Teng, F.; Weng, J.; Zhang, Y.; Fang, X. High-Performance Silicon-Compatible Large-Area UV-to-Visible Broadband Photodetector Based on Integrated Lattice-Matched Type II Se/n-Si Heterojunctions. *Nano Lett.* **2018**, *18* (8), 4697−4703.
(39) Sorifi, S.; Moun, M.; Kaushik, S.; Singh, R. High-Temperature Performance of a GaSe Nanosheet-Based Broadband Photodetector. *ACS Appl. Electron. Mater.* **2020**, *2*, 670−676.
(40) Han, J.; Li, J.; Liu, W.; Li, H.; Fan, X.; Huang, K. A novel flexible broadband photodetector based on flower-like MoS_2 microspheres. *Opt. Commun.* **2020**, *473*, 125931.
(41) Jain, S. K.; Low, M. X.; Taylor, P. D.; Tawfik, S. A.; Spencer, M. J. S.; Kuriakose, S.; Arash, A.; Xu, C.; Sriram, S.; Gupta, G.; Bhaskaran, M.; Walia, S. 2D/3D Hybrid of MoS_2/GaN for a High-Performance Broadband Photodetector. *ACS Appl. Electron. Mater.* **2021**, *3*, 2407−2414.
(42) Vemula, M.; Veeralingam, S.; Badhulika, S. Hybrid 2D/0D $SnSe_2$-SnO_2 vertical junction based high performance broadband photodetector. *J. Alloys Compd.* **2021**, *883*, 160826.
(43) Saraf, R.; Fan, H.; Maheshwari, V. Porous perovskite films integrated with Au−Pt nanowire-based electrodes for highly flexible large-area photodetectors. *npj Flexible Electron.* **2020**, *4*, 30.
(44) Lim, S.; Ha, M.; Lee, Y.; Ko, H. Large-area, solution-processed, hierarchical $MAPbI_3$ nanoribbon arrays for self-powered flexible photodetectors. *Adv. Optical Mater.* **2018**, *6*, 1800615.
(45) Wang, T.; Hou, S.; Zhang, H.; Yang, Y.; Xu, W.; Ao, T.; Kang, M.; Pan, G.; Mao, Y. Highly controllable synthesis of $MAPbI_3$ perovskite nanocrystals with long carrier lifetimes and narrow band gap for application in photodetectors. *J. Alloys Compd.* **2021**, *872*, 159589.

https://doi.org/10.1021/acs.nanolett.2c01979
Nano Lett. 2022, 22, 6655−6663